MASTER THESIS

A Far-Infrared Beam-Steering Offner Relay for SAFARI

Ellen Schallig[a]

Supervisors:
DR. Gert de Lange[b]
PROF. DR. Scott Trager[a]

8th June 2015

[a]Kapteyn Institute, University of Groningen, Groningen, The Netherlands
[b]SRON, Netherlands Institute for Space Research, Groningen, The Netherlands

Abstract

The SAFARI instrument for the SPICA satellite that will be sensitive to wavelengths between 34 and 210 μm is in its design phase and experimental setups are built to develop ideas for testing the instrument during the building phase. An experimental Offner setup was built and calibrated for the purpose of testing the detector arrays that were proposed in the original instrument. The setup is (almost) without misalignment, which was verified with QCL measurements.

Measuring in the far infrared is difficult, as it is challenging to optimize source strength, detector sensitivity, and source and detector diameters at the same time. The most important question is whether an image of a point source can be translated laterally in the focal plane with this Offner setup, without introducing aberrations. This is almost certainly possible, but it is wise to investigate this further.

Contents

1. Introduction

Scheduled to be launched in the late 2020s or early 2030s, SPICA, the Japanese SPace Infrared telescope for Cosmology and Astrophysics is an infrared mission that will look at wavelengths between 5 and 210 μm.

SPICA will have a 3 meter class telescope and will be cooled to a temperature of about 6 K (Goicoechea and Nakagawa, 2011). In the original proposal the telescope will have four instruments in its prime focus: FPC, the Focal-Plane Camera for Guider/Science; SCI, the SPICA Coronagraph Instrument; MCS, the Mid-IR Camera and Spectrometer; and SAFARI, the SPICA FAR-infrared Instrument (JAXA, 2014).

SAFARI is the European contribution, and is being developed under the leadership of SRON, the Netherlands Institute for Space Research. It will have a continuous spectroscopic capability from 34 to 210 μm and simultaneous broadband photometry in three bands in this range. All images will be obtained with background limited accuracy and will be used to study among other things galaxy formation and the formation of planetary systems (SAFARI fact sheet, 12 June 2013), (Swinyard, 21 May 2014).

This research focuses on a test setup for the SAFARI detector arrays as proposed in the original instrument. More precisely, it focuses on the possible use of a beam-steering Offner relay for the characterisation of spatially Nyquist sampled detectors. With the setup a representative Point Spread Function (PSF, the response of the imaging system to a point source) can be generated, and with the aid of a beam-steering mirror this PSF can be moved within the focal plane, similar to the movement of a real PSF in the final instrument when the instrument is scanning the sky.

The Offner relay is a well-known and well-tested system in the visible and near-infrared part of the spectrum (see e.g. Murphy (1994), Fischer et al. (2003), and Prieto-Blanco et al. (2006)), but not much research has been done regarding the far infrared, in which SAFARI will be sensitive.

In this work some practicalities of the setup are detailed. An alignment procedure is included as appendix A. The limitations of the system in the far infrared are tested in this research, particularly when measuring at room temperature and through air. Room temperature and a non-vacuum environment were chosen because it will make adjusting measurements much easier, even though the final instrument will be cooled to about 20 mK and will operate in a vacuum.

Taking measurements in the far infrared is not a standard procedure. Source strength and the sensitivity of detectors in the far-infrared regime are much less than those in the visible regime. In the visible regime readily available lasers, other sources, and CCDs make achieving an acceptable signal-to-noise ratio much easier than in the far infrared.

Ideally, all astronomical instruments should be diffraction limited. The SAFARI instrument should be this too, and therefore all test facilities should also be diffraction limited. This research is important, because it explores the usefulness of an Offner relay in the context of the far-infrared regime and the diffraction limit.

Based on the known properties of the Offner re-imager and simulations performed with ZEMAX, we expect that the PSF can be laterally translated in the focal plane, without actually changing the PSF itself. The actual performance of a representative Offner system is investigated, where both incoherent sources (black body) and coherent sources (a Quantum Cascade Laser and semiconductor sources) are used.

In the original proposal an imaging array was suggested, but this changed to a grating spectrometer in a subsequent revision. This change happened after most of the work for this research was done, so in this thesis the old situation is taken as starting point. However, some sort of relay still has to be used in combination with a grating spectrometer, and an Offner relay is a good option for this.

2. Background

Diffraction happens when electromagnetic waves encounter a physical, opaque, obstruction. This can be a something around which the light has to bend, or an aperture in an opaque screen. This diffraction manifests itself differently in the near field than in the far field. ‘Near’ and ‘far’ is wavelength dependent: the shorter the wavelength, the farther away the far field is. Near-field diffraction is called Fresnel diffraction, and manifests itself with fringes in the pattern. Far away in the far field these fringes are smoothed out. This is the regime of Fraunhofer diffraction. If a lens or mirror is used, the Fraunhofer regime is brought closer, to the focal plane.

The response of the imaging system to a point source is described by the Point Spread Function or PSF. Due to diffraction this image is always smeared out somewhat. In the ideal system as described below the limiting shape of a PSF is an Airy pattern. Measurements of the actual PSF and comparison to this ideal shape are used to characterize the quality of an optical system, to determine the optical resolution. The information below about the ideal Airy pattern is taken from chapter 10 of Hecht (2002).

2.1 Ideal system: Airy Pattern

The Fraunhofer diffraction pattern that is created by a circular aperture that is uniformly illuminated is called an Airy pattern. Imaging far-away point sources (e.g. stars) with ideal imaging systems results in Airy patterns. This pattern consists of a central maximum, surrounded by alternating minima and maxima. It is radially symmetric.

The irradiance I of the Airy pattern at any point is:

$$I(\theta, \lambda) = I(0, \lambda) \left[\frac{2J_1\left(\frac{\pi D}{\lambda}\sin\theta\right)}{\frac{\pi D}{\lambda}\sin\theta} \right]^2, \tag{2.1}$$

where D is the diameter of the circular aperture, λ the wavelength of the light, and θ the angle between the axis of symmetry of the system and the line between aperture center and observation point. This is shown more clearly in figure 2.1. $J_1(u)$ is the first order Bessel function of the first kind.

$I(0, \lambda)$ is the central value given by

$$I(0, \lambda) = \frac{\pi P_{\text{ex}}}{4\lambda^2 F^2}, \tag{2.2}$$

and P_{ex} is the power across the exit pupil, or the power that leaves the optical system and F is the f-number of the system, $F = f/D$, with f the focal length of the objective and D the again the diameter of the aperture. Plots of the Airy pattern can be seen in figure 2.2.

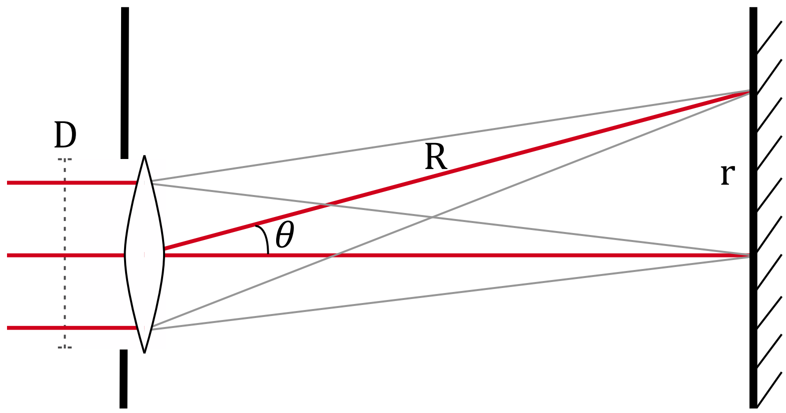

Figure 2.1: Fraunhofer diffraction with an optical system. D is the diameter of the circular aperture, r is the radial distance from the optical axis to the observation point. R is the line from the aperture center to the observation point and θ is the angle between the optical axis and line R.

We say that two point sources (of equal source strength and with the same wavelength) can be barely resolved if the central maximum of one pattern overlaps with the first minimum of the other pattern. This is called the Rayleigh criterion. If a system is able to distinguish two sources that satisfy the Rayleigh criterion, it is said to be diffraction limited. One can compute the angle between these two points by finding the first minimum of one pattern, so where $J_1(u) = 0$. This happens for $u \approx 3.83$. From this we get $\frac{\pi D}{\lambda} \sin\theta \approx 3.83$ and finally, for small angles:

$$\theta \approx 1.22 \frac{\lambda}{D}. \tag{2.3}$$

Equation 2.3 can then be converted to spatial resolution, and the resulting equation for the limit of resolution is:

$$\Delta l \approx 1.22 \frac{f\lambda}{D} = 1.22 F\lambda. \tag{2.4}$$

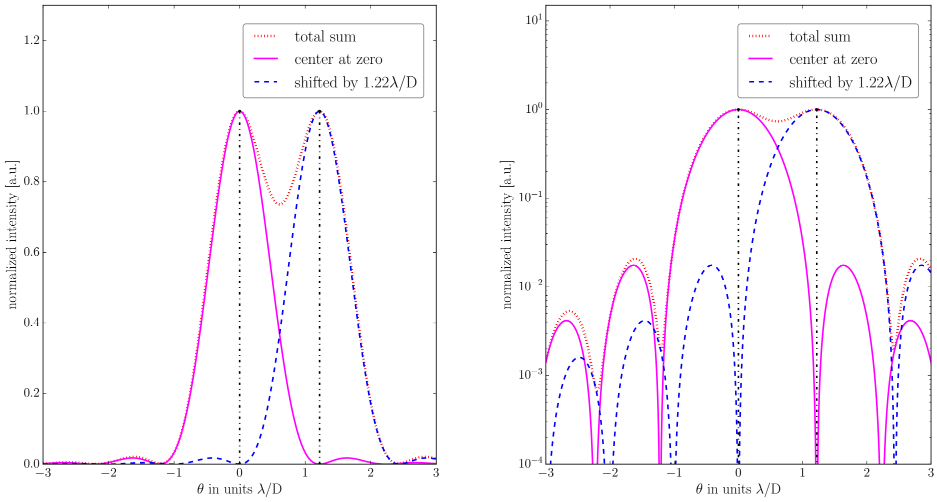

(a) (b)

Figure 2.2: Two Airy patterns with the Rayleigh distance between them. The dotted (magenta) function is shifted by $1.22\lambda/D$ with respect to the solid (blue) function. The maximum of the dotted function is exactly over the first minimum of the solid function. The location of the maxima and minima can be seen more clearly in the log plot in (b).

With this in mind we can also express the irradiance in terms of Fλ:

$$I(\theta, \lambda) = I(0, \lambda) \left[\frac{2J_1(\pi r/F\lambda)}{\pi r/F\lambda} \right]^2, \tag{2.5}$$

with r the radial distance from the optical axis, shown in figure 2.1, and $I(0, \lambda)$ unchanged from equation 2.2.

The telescope that will collect the light for SAFARI will be diffraction limited. This means that the imperfections in the system will have to be small enough that the aberrations from those imperfections will not make θ larger than the Rayleigh criterion. In a telescope the measured PSF will differ from the Airy pattern because of the effects of the central blockage and struts of the secondary. This results in the well-known star shaped PSF.

A two-dimensional Airy pattern, of which a cross-section is actually measured, is shown in figure 2.3.

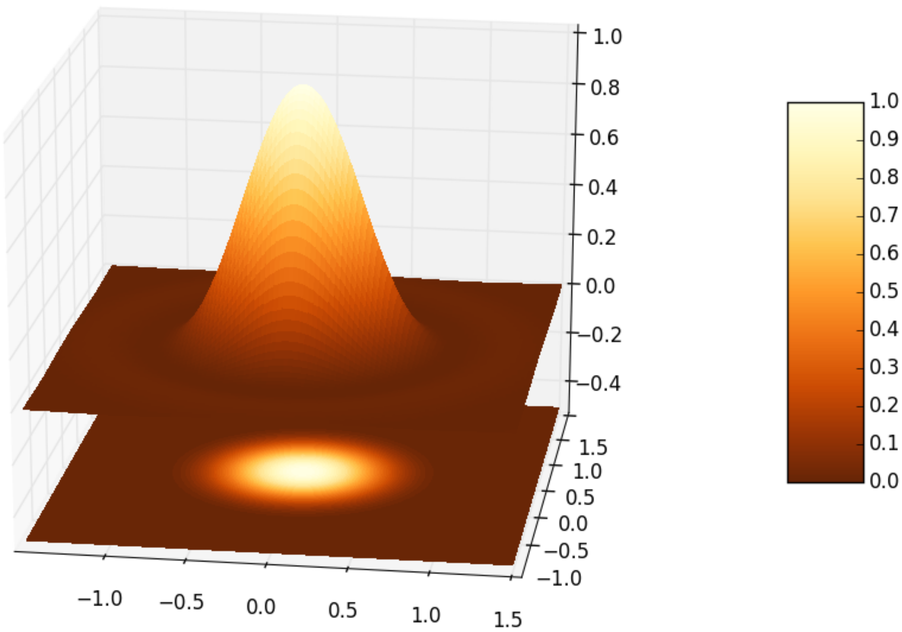

Figure 2.3: Two-dimensional Airy pattern with normalized intensity. A contour plot is shown below. Still visible is the second maximum, which manifests itself as a ring around the Airy disk.

2.2 Nyquist Sampling

To make full use of the diffraction limited system, SAFARI's detectors can be at most a certain size. To be able to distinguish between two peaks, the dip in the center between them has to be detected too. This is called Nyquist sampling. With a maximum resolution of 1.22 $F\lambda$ (equation 2.4) this means that the individual detectors can be at most 0.61 $F\lambda$ apart. It is common to refer to this spacing as 0.5 $F\lambda$, to make the spatial sampling distance strictly smaller than the Nyquist sampling distance and achieve unambiguous representation of the signal. In SAFARI the half band wavelength is used as the sampling wavelength, which strictly speaking causes half of the wavelength band to be oversampled, and the other half to be undersampled. The f-number of the system will not change.

In figure 2.4 a Nyquist sampled monochromatic Airy pattern is plotted. The central pixel is positioned on the center of the Airy pattern. The central pixel gets 28% of the total intensity, the central 5 pixels get 69%, and the central 9 pixels get 84%.

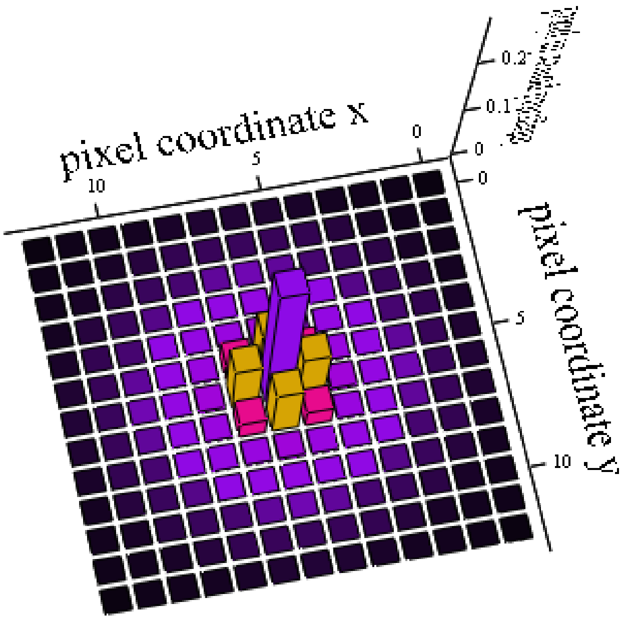

Figure 2.4: Two-dimensional Airy pattern with normalized total intensity, Nyquist sampled with square pixels. Each side of the pixel is $0.61F\lambda$. The central 5 pixels catch almost 70% of the total intensity.

2.3 Polychromatic Sources

Most sources are not monochromatic, but generate light in broader bands of wavelengths. The observed objects for SPICA can be considered as far away point sources, but they will never be monochromatic. This will influence the resulting PSF, as the Airy patterns of each wavelength are combined to get the resulting pattern. For sources that emit only in small bands the zeros in the individual Airy patterns are close enough that a dip is still visible in the resulting pattern. However, for broader bands, the zeros are so spread out that the resulting pattern is also smeared out, and you can see only a general reduction of the pattern the farther you go away from the center.

The PSF of polychromatic sources can be calculated by integrating formula 2.1 over λ:

$$I(r) = I(0) \int_{\lambda_1}^{\lambda_2} \frac{1}{\lambda^2} \left[\frac{2J_1(\pi r/F\lambda)}{\pi r/F\lambda} \right]^2 d\lambda. \tag{2.6}$$

The factor $1/\lambda^2$ is taken from $I(0, \lambda)$ in equation 2.2. λ_1 and λ_2 are the edges of the wavelength band that is integrated over. Examples of polychromatic PSFs can be found in figure 2.5, where a monochromatic PSF is compared to multiple polychromatic PSFs.

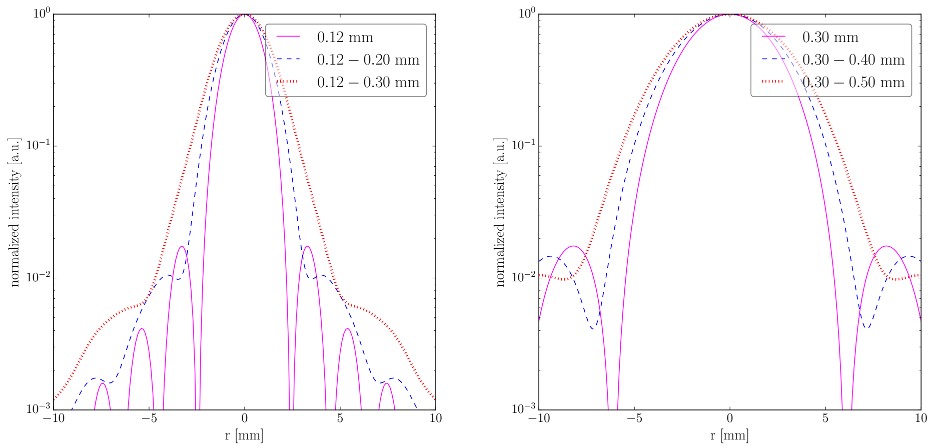

(a) Shorter wavelengths. (b) Longer wavelengths.

Figure 2.5: The PSF is smeared out when larger wavelength bands are used in the measurements. One can also see clearly that the distance to the first minimum is dependent on wavelength.

2.4 Extended Sources and Detectors

In the past sections the source was characterized as a perfect point source which is subsequently detected as an Airy pattern. However, this is only part of the picture. Ideally the source and detector are both infinitely small pinholes, but these would not be able to emit or absorb radiation. Since we have to deal with the finite size of the detector and the source, we have to take into account the convolution of the ideal PSF with both the source and the detector. The optics are still assumed to be perfect. If the system is diffraction limited, this is a good approximation, as the influence of non-ideal optics are negligible compared to the diffraction.

The source and the detector will 'blur' the measurement, with the amount of blurring or smearing dependent on the size of the source and detector. The following paragraphs on how to deal with extended sources or images of incoherent disks are described in much more detail in Mahajan (2011), in particular lecture 9 in the series. The specific inputs for the images in this section are also based on the images in lecture 9.

In the section below we make use of the Gaussian image in the Fourier transform: an aberration-free image based on geometrical optics only. Therefore the image is a scaled image of the original, and in this case the magnification is 1.

The image of a radiating pinhole with an extended size can be found by convolving the Gaussian image of the pinhole with the PSF of the imaging system. This operation can also be performed with Fourier Optics in the spatial frequency domain by making use of the Optical Transfer Function (OTF) and the spatial frequency spectrum of the extended pinhole. If the aperture of a detector that is scanned across the image also is extended, another convolution of the image of the pinhole with the aperture of the detector is necessary. This can also be included as a multiplication in the spatial frequency domain. From the analysis as given in Mahajan (2011, lecture 9) it can be concluded that if the radius of the pinhole is smaller than $0.25F\lambda$ the pinhole can be considered a point source.

Here the source is modelled as a uniformly radiating disc with radius h_g. These two functions multiplied and inverse Fourier transformed yield the image. For a monochromatic aberration free system with a circular pupil the OTF is (Mahajan, 2011, lecture 3):

$$\tau(\nu) = \frac{2}{\pi}\left[\cos^{-1}\nu - \nu\left(1-\nu^2\right)^{\frac{1}{2}}\right], \tag{2.7}$$

and the spectrum of the Gaussian image (Mahajan, 2011, lecture 9):

$$\widetilde{I}_g(\nu_i) = P_{ex}\frac{2J_1(2\pi\nu_i h_g)}{2\pi\nu_i h_g}, \tag{2.8}$$

with P_{ex} the power in the exit pupil and therefore in the image, ν_i the image spatial frequency, h_g the radius of the image, and ν the normalized image spatial frequency with

$$\nu = \frac{\nu_i}{1/F\lambda}. \tag{2.9}$$

Because of the factor $1/F\lambda$, ν can at most be 1. Let I_g be the irradiance of the Gaussian image, and b_g the radius in units of $F\lambda$: $b_g = h_g/F\lambda$. Transforming the convolution back to real space we get:

$$I_i(r) = 2\pi I_g b_g \int_0^1 J_1(2\pi\nu b_g)J_0(2\pi\nu r)\tau(\nu)d\nu. \tag{2.10}$$

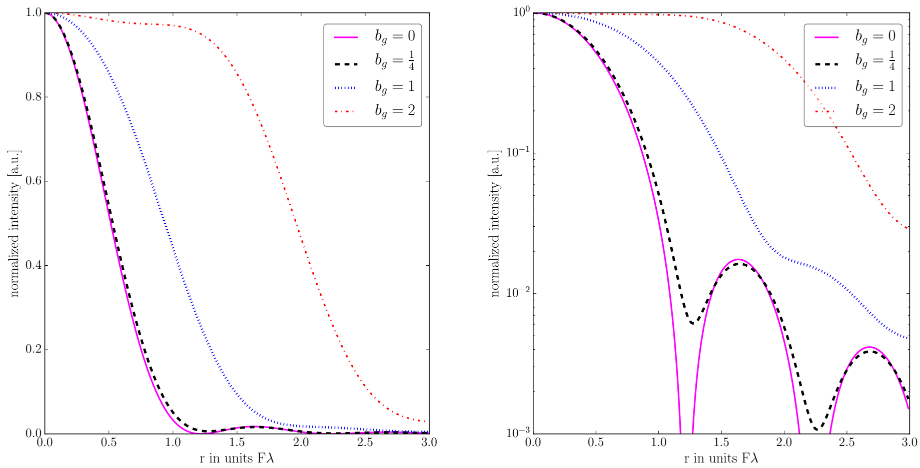

(a) Normal y axis (b) Logarithmic y axis

Figure 2.6: Influence of extended source on Airy pattern. Larger image radius ‘blurs’ the pattern. Radius in terms of $F\lambda$. A source with radius $b_g = 1/4$ can still be treated as a point source. See also Mahajan (2011, lecture 9).

This is the equation for an incoherent extended source imaged with a perfect detector that does not sample the measurement. Corresponding graphs are found in figure 2.6, and analysis shows that a source (or detector) with radius $0.25F\lambda$ can indeed still be treated as a point source.

If the detector has a circular opening with a radius larger than this $0.25F\lambda$, it can be treated the same way as the extended source. Now instead of taking h_g as the radius of the extended image, we use h_d for the radius of the detector opening, and b_d as the radius in terms of $F\lambda$: $b_d = h_d/F\lambda$:

$$I_i(r) = 2\pi I_g b_g b_d \int_0^1 \frac{J_1(2\pi\nu b_g) J_1(2\pi\nu b_d) J_0(2\pi\nu r)}{\nu} \tau(\nu) d\nu. \tag{2.11}$$

Figure 2.7 shows the influence of the source and detector together. Widening of the central maximum occurs very easily, and this will be an important factor in explaining the measurements in chapter 4.

Equation 2.11 can also be used for polychromatic light. In this case $\tau(\nu)$ is not the OTF for monochromatic light as in equation 2.7, but rather (Mahajan, 2011, lecture 9):

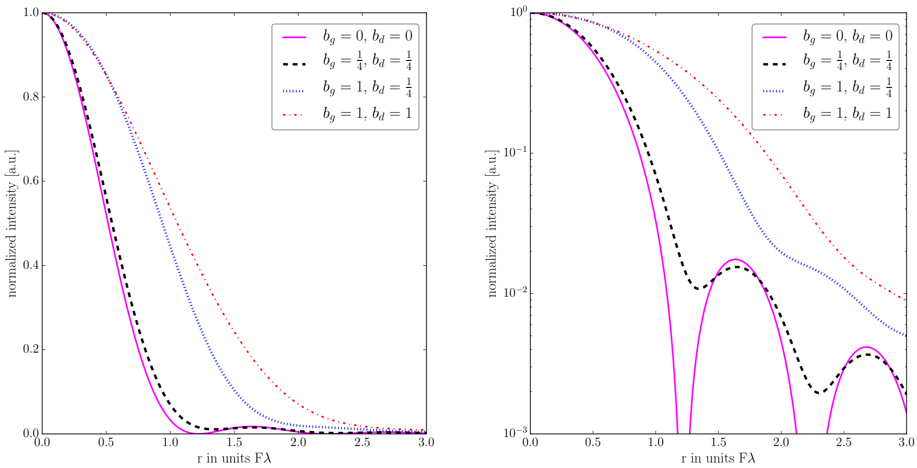

(a) Normal y axis

(b) Logarithmic y axis

Figure 2.7: Influence of extended source and larger detector opening on Airy pattern. Larger radii 'blur' the pattern. Radii in terms of $F\lambda$.

$$\tau_p(\nu) = \frac{2}{\pi(q-1)} \int_1^q \left[\cos^{-1}(x\nu) - x\nu\left(1 - x^2\nu^2\right)^{\frac{1}{2}}\right] \mathrm{d}x, \tag{2.12}$$

where $q = \lambda_{\text{max}}/\lambda_{\text{min}}$ denotes the bandwidth of the system, and $x = \lambda/\lambda_{\text{min}}$. ν is now defined as $\nu_i F \lambda_{\text{min}}$, instead of equation 2.9.

Equation 2.12 only works if the factor $x\nu$ in the $\cos^{-1}$-term and in the square root remains smaller than or equal to 1. This only happens for $q = 1$, so in all other cases where $x\nu > 1$ the integrand is defined as 0. In figure 2.8 the kinks in the curves for $q > 1$ are explained by this.

2.5 Atmospheric Influence

In the last sections it was established that the final shape of a measured polychromatic PSF depends on the optical quality of the system, the spectral emission and bandwidth of the source, and the spectral response and bandwidth of the detector.

These are not the only things that impact the quality of the image. The medium in between the source and detector is also important, particularly the filtering properties. In air, certain atoms and molecules absorb parts of the spectrum and make these wavelengths impossible to use for analysis. Especially in the mid- and far-infrared the water molecules in the Earth atmosphere

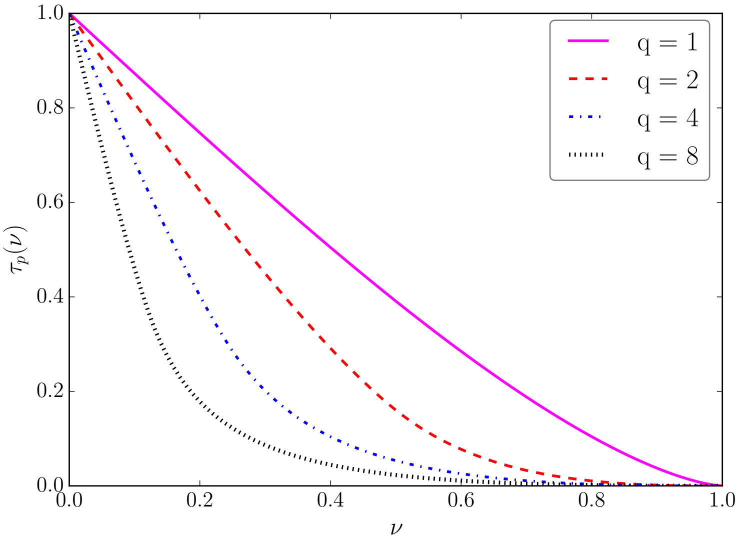

Figure 2.8: The polychromatic OTF for normalized ν. $q = 1$ is the monochromatic case that reduces to equation 2.7. Visible light has $q = 0.7\ \mu\text{m}/0.4\ \mu\text{m} = 1.75$. Most detectors should have $q \leq 3$; the curves of $q = 4$ and $q = 8$ are for illustration purposes only.

have high absorption. This is shown in figure 2.9, with a large wavenumber ν corresponding to a large frequency: $f = c\nu$. The source in use for the measurements is a globar which approximates a black body.

The figure shows quite clearly that the atmosphere is transparent in certain wavelength bands only, and certain wavelengths come through much stronger than others. This coupled with the source emission and detector response will give us much information on which wavelength bands can be excluded from the analysis.

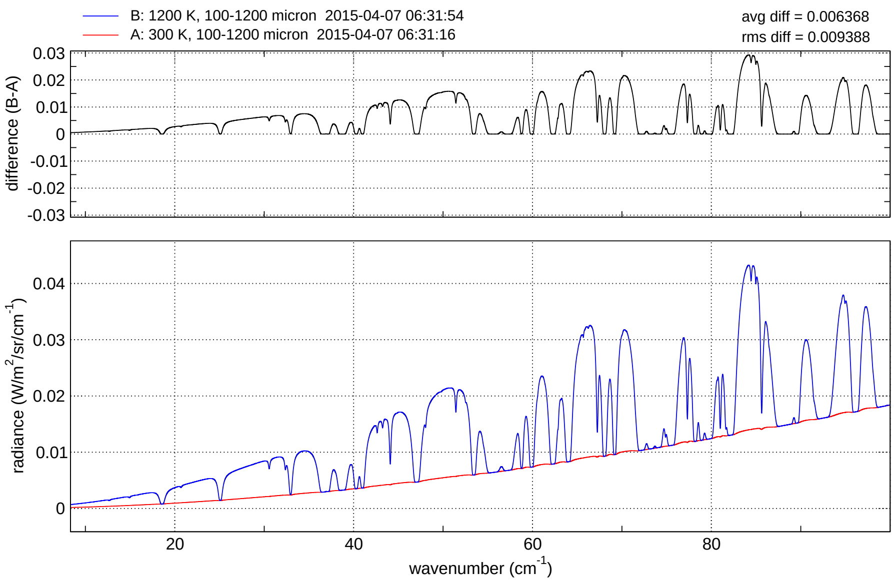

Figure 2.9: Theoretical spectra of black-body radiation with a pathlength of 3 m air between the globar and the detector. The temperatures of 1200 K (blue) and 300 K (red) are the approximate temperatures of the globar and the lab. The black curve shows the difference between both spectra, which can be compared to measurements in the lab. Made with atmospheric path plotting tools on `http://spectralcalc.com`.

3. Experimental Setup

In 1973, Offner patented a catoptric system that forms an image of an object at unit magnification, free of spherical aberration, coma and distortion, with possibilities of making the image free of third order astigmatism and field curvature as well. This system consists of two spherical mirrors: a concave and a convex mirror. The convex mirror has a radius of curvature half of that of the concave mirror. This is now commonly called an Offner setup, and the original sketch of the setup can be seen in figure 3.1. For moderate apertures and fields, this system provides diffraction limited performance.

Another advantage of the Offner system is its compactness. The total distance the light has to travel is folded in such a way that only a third of the total distance is needed for this system. This makes it easier to put the whole system in a test cryostat (not in this research).

Lastly beam steering is possible by tilting the small mirror a certain angle, which again is advantageous in low temperatures. Instead of having to move the detectors or the source around a fixed beam of light, the light can be moved around. Tip-tilting a small mirror around the two axes of rotation takes much less energy than moving around the source or a complete array of detectors in the xz-plane.

3.1 Offner System Setup

For the setup described in this work an existing large concave spherical mirror (the primary) with a radius of curvature R_l = 1000 mm and a diameter d_l = 350 mm was used. This mirror was available from a previous setup. Two smaller convex spherical mirrors (the secondaries) were used sequentially, both with a radius of curvature R_s = 500 mm, as dictated by the Offner setup. Figure 3.2 shows a sketch of this setup. The first secondary mirror, again available from a previous experiment, has a diameter of d_{s1} = 70 mm. The second one has d_{s2} = 30 mm and was designed to give a representative f-number of 16.7, as was proposed in the SAFARI instrument description. All mirrors can reflect light in both the submillimeter and the visible regime. The optical quality helps with optical alignment of the setup, as a visible light source such as a theodolite can now be used.

Alignment was done with a theodolite on an xz-stage which can move the theodolite up (z) and laterally across the mirrors (x), a few plane mirrors,

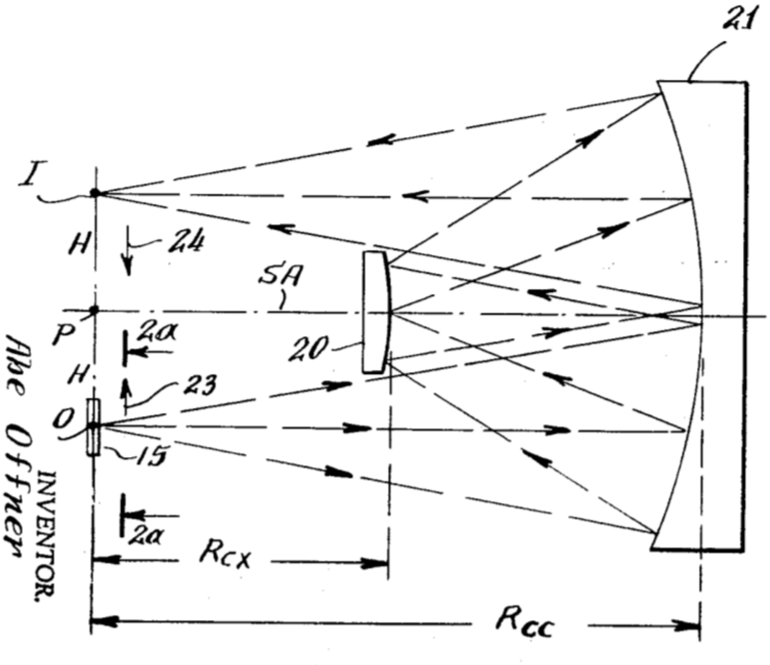

Figure 3.1: Sketch of one of the embodiments of Offner's patent (Offner, 1973). The centers of curvature coincide at point P. R_{cc} and R_{cx} are the radii of curvature of the concave and convex mirror, respectively. R_{cc} is twice the radius R_{cx}.

a collimated beam of light, and a pointing mechanism (in this case: a pen on a stick). The coordinate system for this setup is found in figure 3.3. The spherical mirrors were secured to an optical table. For alignment the centers of curvature of both mirrors and the principal axes should overlap. It is assumed that the back of the primary mirror is planar and tangent to the principal axis. The complete procedure for alignment can be found in appendix A.

The tip and tilt of the beam-steering secondary mirrors are guided with a small computer program. The larger secondary mirror was used until the end of February 2014, the smaller one was used from the start of March 2014. The measurements discussed in chapter 4 are made only with the smaller secondary.

3.2 Hardware

The complete setup consists of not only the two mirrors that make up the Offner relay, but also of various sources and detectors. The secondary mirror

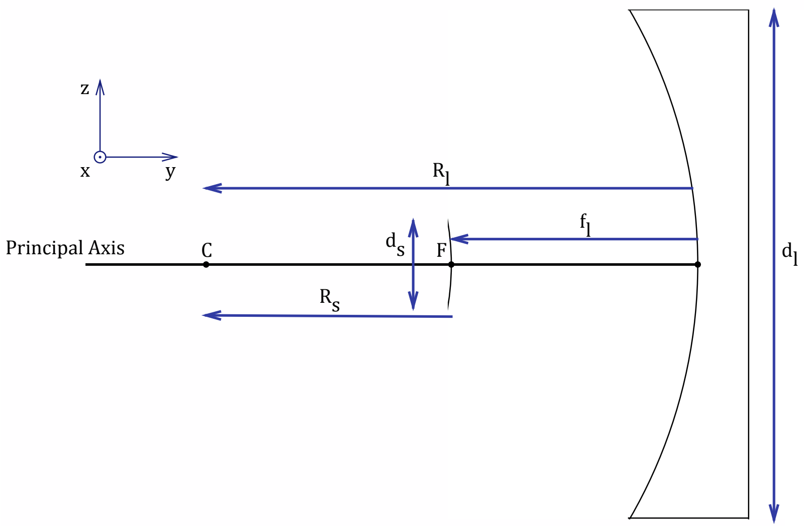

Figure 3.2: Properties of the system. The subscript l denotes properties of the large mirror, s indicates the small mirror. C is the center of curvature, F is half the distance to the large mirror, and therefore the focal point of the large mirror and the point where the small mirror should be positioned. Note the coordinate system: y is towards the primary, z is up, and x is out of the paper.

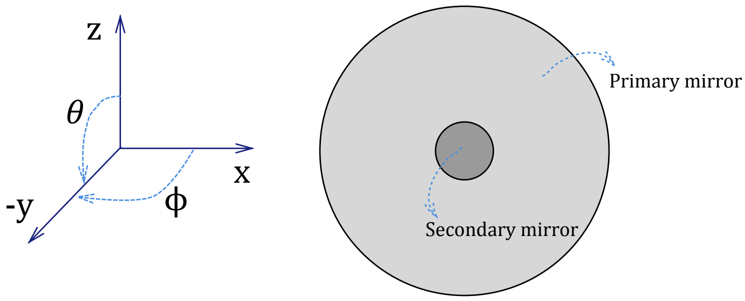

Figure 3.3: Coordinate system with the mirror orientations as reference, where the small mirror is seen from the back. z is upwards, x to the right and y towards the mirrors. θ is the angle in the yz-plane, ϕ is the angle in the xy-plane.

(figure 3.4 (b)) is controlled by an attocube system, a goniometer powered with piezo motors that makes very small and precise steps possible. The total path length the light must travel is 3.0 m, as R_l = 1000 mm (figure 3.2) is travelled twice, and f_l = 500 mm is also travelled twice.

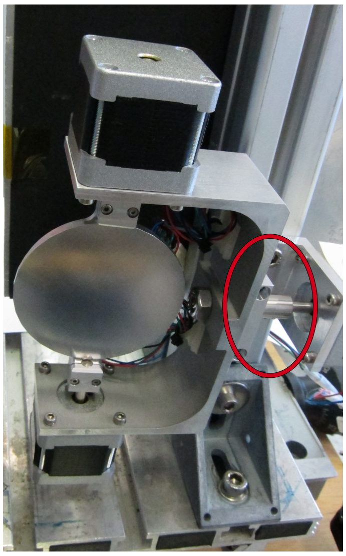

(a) The mirror in use until the end of February, with $d_{s1} = 70$ mm. The mirror was polished after this photo was taken.

(b) The secondary mirror in use from March, with $d_{s2} = 30$ mm.

Figure 3.4: The secondary mirrors. The hanging mechanism for the first mirror is to its side, therefore the back of this mirror can be used in the alignment. For this see appendix A.

The secondary mirror in figure 3.4 (a) was controlled by a set of stepping motors which were not very precise and could not make sufficiently small steps. After acquirement of the attocube system the stepping motors and this secondary were not used anymore.

The source is a globar normally powered with 4.92 A, very occasionally with 5.75 A. This last amount is not sustainable for long times, as it will cause small damage over time to the globar. This corresponds roughly to a 1200 K black body.

A helium-cooled bolometer detects the light. All measurements are taken with the 100 cm^{-1} low-pass filter, so only light with frequencies up to 3.0 THz is detected by the bolometer. This is a compromise between available power, pinhole size, and size of the Airy disk, discussed in more detail in chapter 4.1.

A lock-in amplifier is used to extract the signal from the bolometer. This can only be done if a carrier frequency is introduced in the signal, which is done by 'chopping' the signal up with a chopper, that intersperses the true signal with a different signal. In this case the different signal is from the ambient temperature, 300 K.

Lastly, different metal diaphragms are used to control the source and detector opening sizes. However, during initial measurements the diaphragms attached to the source heated up and started radiating as well. Together with a chopper that was placed in between the pinhole and the mirrors (instead of between the source and the pinhole), this explains the features that were seen initially. These looked like smeared out Airy patterns at first glance, but were actually something different. The chopper was chopping the signal plus the radiation from the heated diaphragm, because it was placed between the pinhole and the mirrors. However, chopping the signal before it went through the pinhole proved to be difficult, as the built-in chopper did not have a stable chopping speed and other choppers could not be built in.

The 'wings' in the measurements in chapter 4 are explained by these metal diaphragms. The different heights the wings attain in these measurements can be explained by the different amounts of time the source was on, and therefore how much time the diaphragms had to heat up. This problem was solved in follow-up measurements that took place in the autumn and winter of 2014.

3.3 Calibration of Steering Mechanism

After the alignment procedure, the calibration of the secondary mirror's steering mechanism was checked. For the attocube system different calibration files can be loaded dependent on the exact configuration and usage of the attocube. One can check manually whether the correct calibration file is loaded by computing the angle the mirror should have for a given distance s, which is the extra distance from C in figure 3.5 due to the angle of the secondary.

In the line of reasoning below it is assumed that for light rays with small width, a curved mirror can locally be assumed flat. Therefore the angle of incidence is the same as the angle of reflection.

In figure 3.5, in the asymmetric case the angle of incidence is $2\alpha+\beta$. Therefore the angle of reflection is also $2\alpha + \beta$, and the angle between the light ray and the optical axis is $2\alpha + 2\beta$. Because the light ray and the principal axis are parallel, the interior angles are equal. This means that the angle of reflection is half of this, and thus $\alpha + \beta$.

For the final result the small angle approximation is used, where $\sin(x) \approx x$, with x in radians:

$$\begin{aligned} d &= R\sin(\alpha) \\ d + s &= R\sin(\alpha+\beta) \\ s &= R\sin(\alpha+\beta) - R\sin(\alpha) \\ s &\approx R\beta. \end{aligned} \tag{3.1}$$

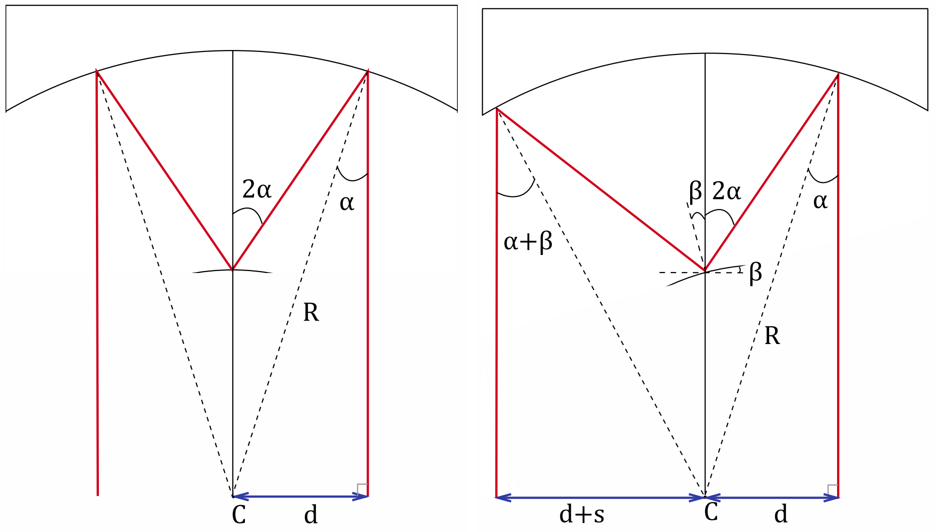

(a) Symmetric case (b) Asymmetric case

Figure 3.5: In situation (a) the secondary is not angled away from the primary in any way. In situation (b) an angle β is introduced, which ultimately defines how much the light is translated laterally in the xz-plane.

So the angle β directly gives the translation s in the xz-plane for a given setup with a primary radius of curvature R.

The attocube system measures the angle of the secondary mirror in millidegrees. This angle β can be converted to an angle in degrees α in the following way: $\beta = \pi\alpha/180$. With $R = 1000$ mm in the Offner setup the conversion from millidegrees to millimeters then becomes:

$$s \approx \alpha \frac{\pi}{180}. \tag{3.2}$$

The factor 1000 is cancelled by the conversion from degrees to millidegrees.

3.4 ZEMAX Software

ZEMAX is an optical design program that uses ray tracing to model the performance of optical systems. After the different components of the system are drawn, called surfaces, rays are traced from one surface to the next. Any ray that is blocked or does not fall on the next surface, will stop being traced. Thus ZEMAX can give a tremendous amount of information even before the system has been built.

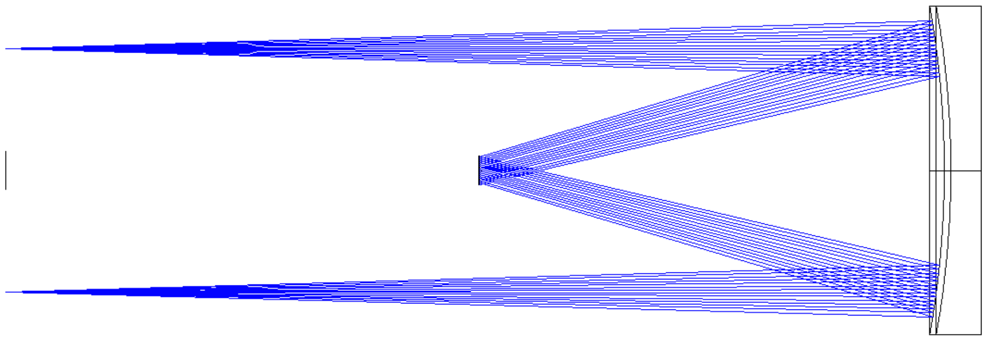

Figure 3.6: Simulation of Offner system as described in section 3.1. Only the light that falls on the secondary mirror is traced.

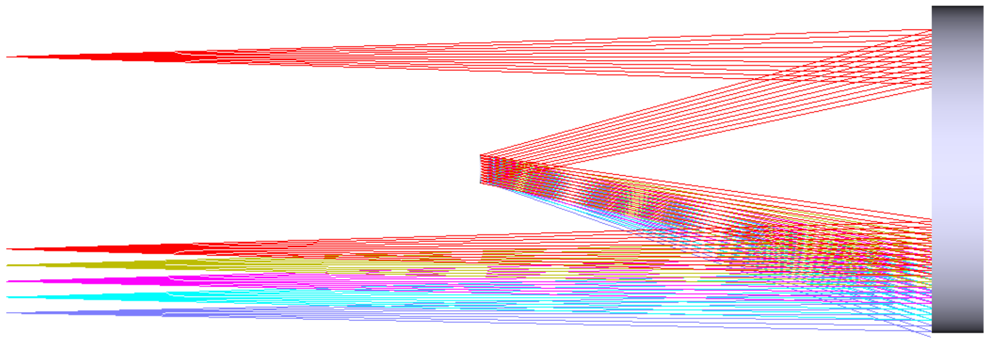

Figure 3.7: By tilting the secondary mirror with respect to the primary, it is possible to shift the beam downwards.

In figure 3.6 the ray tracing is shown. Only the light that falls on all elements is traced to the end. Figure 3.8 shows the ends of these rays on the detector side for two wavelengths: 50 μm and 200 μm. Also drawn are the corresponding Airy disks for these wavelengths. The size of the diffraction limited Airy disk is much larger than the spread of the spots, so it should indeed be possible to build a diffraction limited Offner system. In figure 3.7 the system's capabilities for moving around the PSF is illustrated. It works in theory, and section 4.3 shows that it works in practice as well.

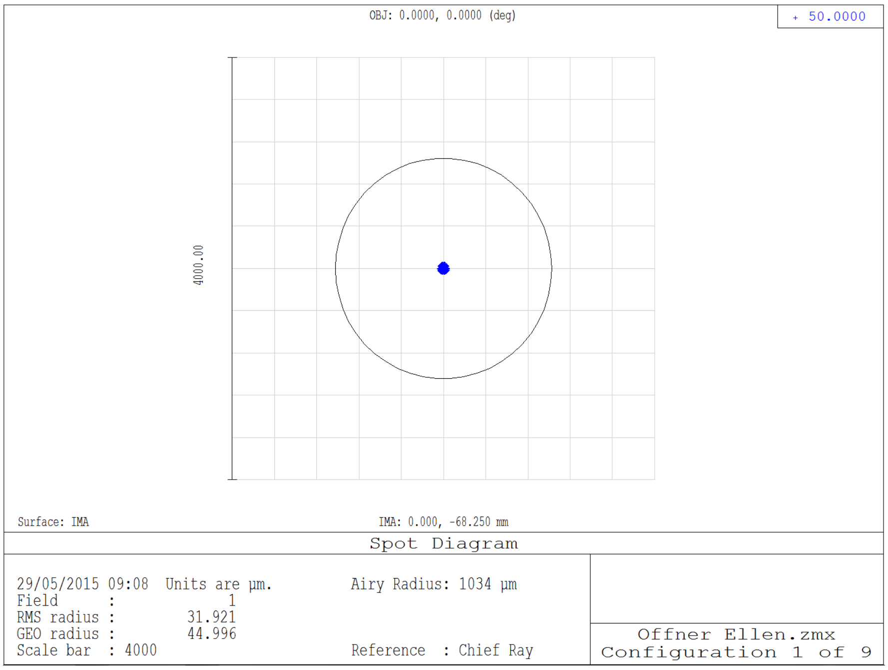

(a) $\lambda = 50$ μm, Airy radius = 1034 μm.

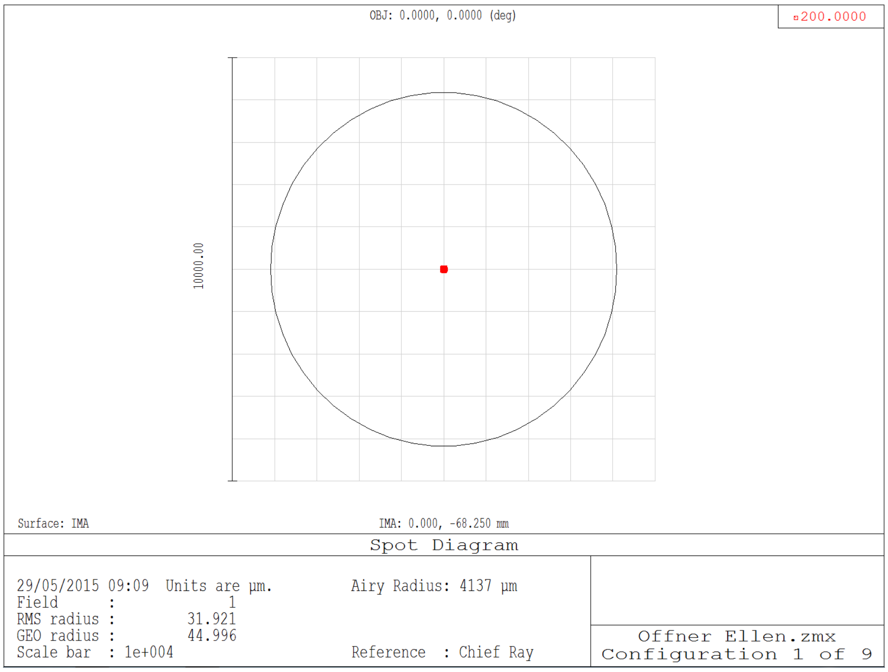

(b) $\lambda = 200$ μm, Airy radius = 4137 μm.

Figure 3.8: Spotdiagrams made with ZEMAX. The spots are where the different rays are traced to on the detector side. Spot spreading is from higher order aberrations inherent to the Offner system. It is clear that these aberrations are much smaller than the Airy disk, which is the diffraction limit.

4. Results

4.1 Atmosphere

Calibration measurements were done with the CRIMI, a Fourier Transform Spectrograph in use by SRON (for more information on the CRIMI see Schallig (2013)). The setup can be seen in figure 4.1, with the CRIMI between the detector and the source (not pictured).

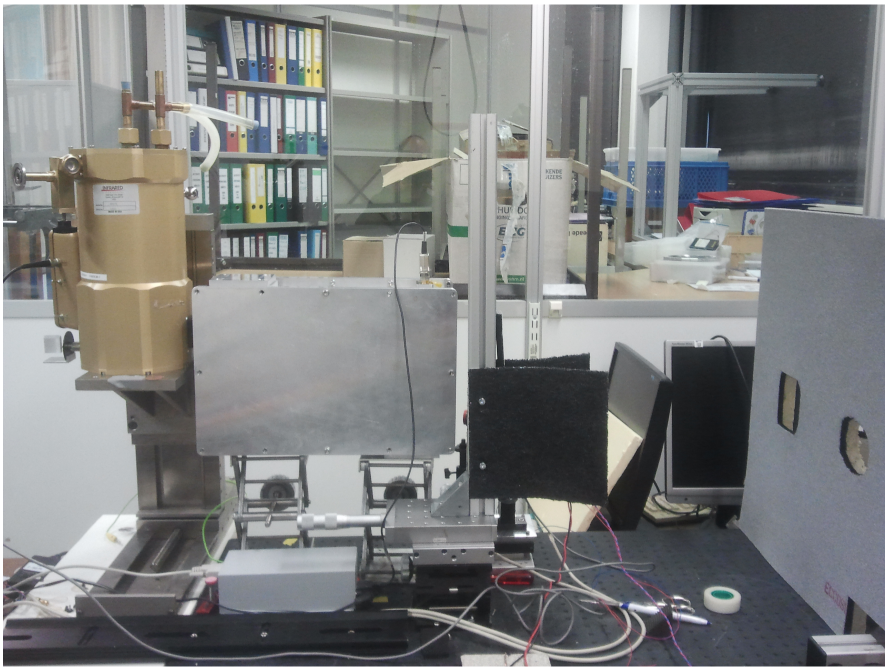

Figure 4.1: Atmospheric measurements with the CRIMI, the gray box to the left of the picture. On the right the mirrors are masked to remove stray light from the measurements.

Three settings on the bolometer are available. The 100 cm^{-1} (100 μm or 3.0 THz) used in this setup is a compromise between available power, pinhole size, and size of the Airy disk. With longer wavelengths (30 cm^{-1}) an Airy disk becomes larger, but the power of the black-body emission becomes so small that the signal-to-noise ratio at the detector is too poor. With the other setting of the bolometer (800 cm^{-1}) much more power is available, but the pinhole size would then have to become very small to get the spatial resolution of the

Airy pattern. The source is a globar with a temperature of around 1200 K, and can be modelled as a black body.

With this setup not only the transmission of the atmosphere was measured, but also the combined responsivity of the detector and the extent to which the source emits as a black body. In figure 4.2 this measurement is plotted together with the theoretical atmospheric spectrum obtained in section 2.5.

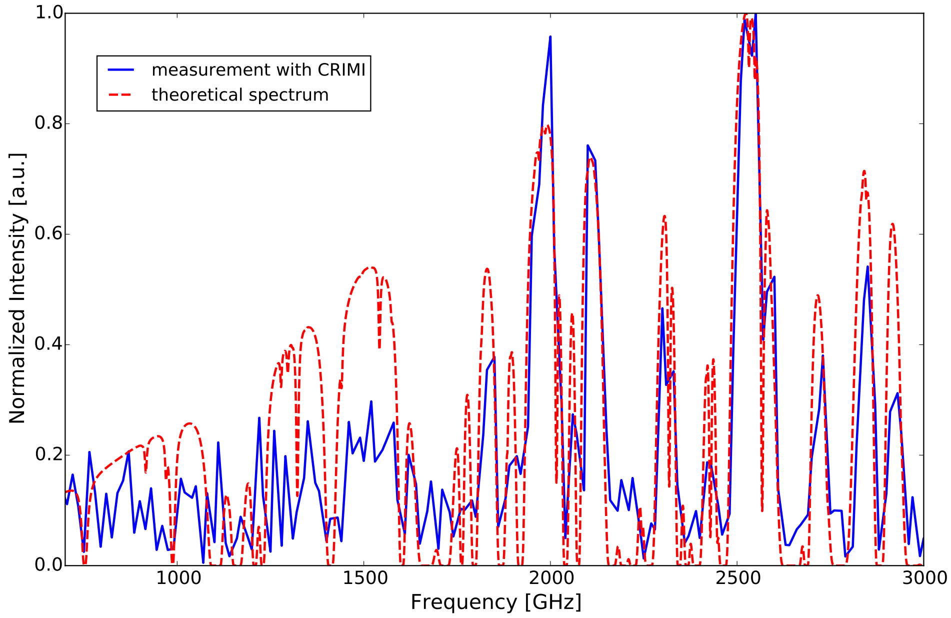

Figure 4.2: Normalized spectra. The red spectrum is the difference between a 1200 K and 300 K black-body spectrum as detailed in figure 2.9, the blue spectrum is the measurement from the CRIMI FTS.

The measurement and theoretical spectrum agree well, particularly in the frequencies around 2.0–3.0 THz. The discrepancies up to 1.5 THz can be explained by a source that does not perfectly radiate like a black body, and possibly by the responsivity of the FTS and the detector. This result means that the discussion of the polychromatic patterns can be simplified to a few discrete frequencies, namely 2.0, 2.1, and 2.5 THz (0.15, 0.14, and 0.12 mm).

4.2 QCL Measurement

After the experimental work of this thesis was finished, the measurements continued and a coherent narrowband Quantum Cascade Laser (QCL) with a frequency of 3.91 THz was obtained. A measurement done with this source can

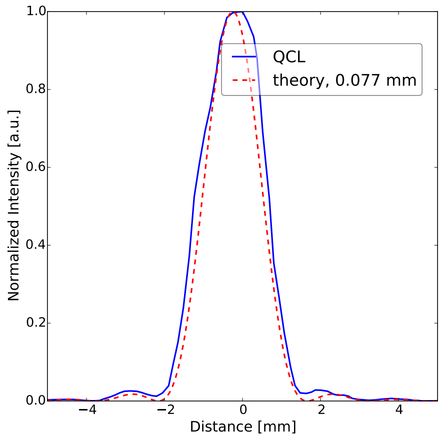

(a)

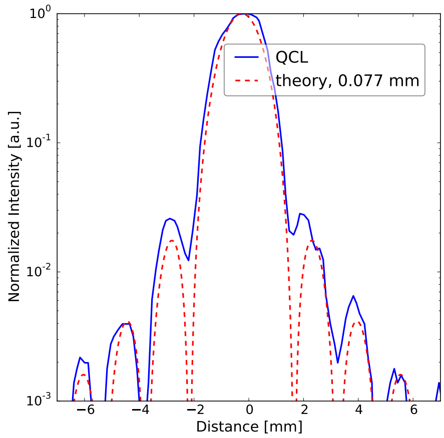

(b)

Figure 4.3: Normalized spectra. The red spectrum is the theoretical Airy pattern for $\lambda = 0.077$ mm, or 3.91 THz, blue is the measured spectrum with a QCL source of 3.91 THz.

be seen in figure 4.3. The close resemblance with the theoretical Airy pattern shows that the experimental Offner setup indeed has a (close to) diffraction limited performance at the wavelengths of interest. The differences between the theoretical curve and the experimental curve could be due to slight misalignment (defocus) and/or the specific phase front of the QCL. This is under further study. For shorter wavelengths the alignment becomes progressively more critical.

With a coherent high power point source as the QCL, details of the optical performance can be easier verified than with the broadband, low-power globar source. The effects of the extended size of the source and the polychromatic smearing of the point source are not present. On the other hand the real objects of observation will be polychromatic and possibly extended, so a good understanding and interpretation of polychromatic imaging as described in this thesis is necessary.

4.3 Lateral Translation of PSF

The most important question is whether it is possible to move around a PSF or any other shape in the focal plane without distorting that shape.

For this, measurements were taken by tilting the secondary mirror a certain angle in the horizontal direction, with respect to its zero position (aligned with the primary mirror), and then scanning in the horizontal (x) or vertical

(z) direction. With this method a range of 1.8° was converted to a horizontal translation of about 30 mm. The total scanned range is about 50 mm. The raw data can be seen in figure 4.4 (a).

Figure 4.4 (b) shows the same data naively plotted over each other. This is done by shifting the maximum value to zero. As the maximum values measured here are not necessarily the real maximum values, this is a very primitive way to compare the measurements. However, even with only this shifting, it is already clear that the measurements agree very well. This is augmented by the logarithmic y-axis. Only the yellow measurement does not overlap completely. The extra intensity is probably due to scattered light that was not completely blocked out in that area of the primary mirror.

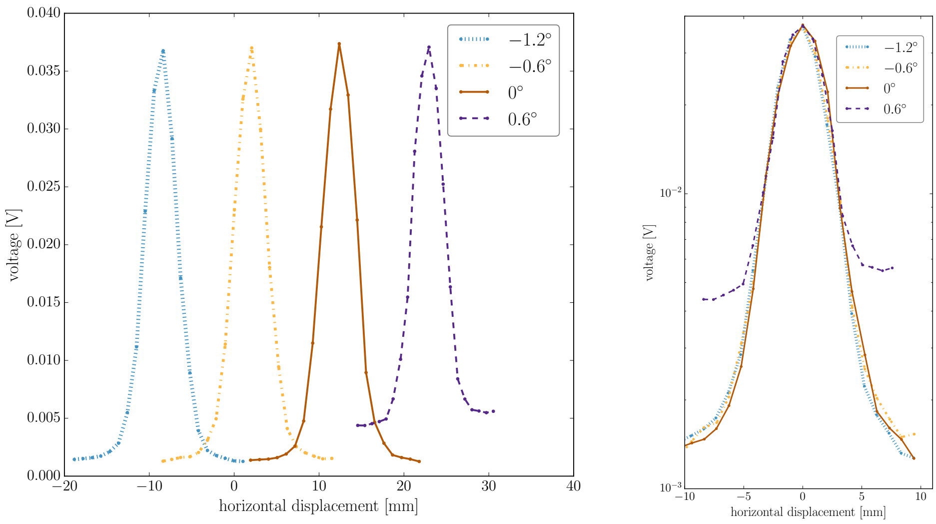

(a) Raw data. (b) Collective center.

Figure 4.4: Beam-steering measurements in the horizontal direction.

From these measurements one could already conclude that the PSF does not change, at least not much. However, quantitative analysis is even more useful. If these measurements were done with a two-dimensional array of square horns, the amount of power collected by each individual pixel would be directly comparable to other pixels. This is approximated by integrating the measurements over intervals that are the same dimensions as the pixels.

The dimensions of the pixels are dictated by Nyquist sampling (section 2.2). Each side of the pixel can be at most 0.6 $F\lambda$ long. For this system with an F of 50/3 and $\lambda \approx 0.15$ mm the pixel size is 1.5 mm. The measurements were taken with a distance of approximately 1.04 mm between each point, which is just better than Nyquist sampled.

For complete accuracy the measurements should be integrated and Nyquist sampled in the xz-plane, not only in one dimension. However, for comparison between the measurements integration along the r-axis suffices, even though the 'power' in this instance is not the total power in a square array, and the 'power' in each one-dimensional pixel will not be the same as the power in a real two-dimensional pixel.

To find the comparable power in each one-dimensional pixel, first the measurement is fitted with a Gaussian curve and centered at zero, and for this fit only the voltage larger than some threshold is selected. In figure 4.4 (a) the yellow curve shows higher wings than the other curves. This is unwanted in the fit, so the threshold is chosen to be 9 mV. These fits are then integrated between the ranges that are dictated by the pixel sizes and normalized by the total power of each fit. The central pixel straddles the peak of the measurement.

This is plotted in figure 4.6. On the left the vertical measurements are shown. While the PSF is only moved horizontally, the vertical direction also has to be checked for aberrations. The measurements overlap so well that it is hard to distinguish between them. On the right the horizontal measurements are shown. These differ slightly more, but this could be due to the Gaussian fits. Taking the data from figure 4.4 (b), but now as a linear plot in figure 4.5 (a), the peaks are all the same height, whereas the Gaussian fits plotted in figure 4.5 (b) differ a bit. It is not much, but after integration this small difference has suddenly become larger. However, to be certain, follow-up measurements should be done that oversample the central peak. This way the actual peak cannot be missed. It will help the computer to fit a curve more accurately if more measurement points are available.

Still, the difference between the horizontal pixels is small, and strongly suggest that it is indeed possible to move a PSF around in the focal plane without changing the PSF itself, in the current setup.

4.4 Pinholes

Section 2.4 deals with the theoretical explanation of the influence of different sizes of the openings on the source and the detector. Ideally one would have point sources and pinholes, but this is not feasible in reality, as it would be impossible to get a decent signal-to-noise ratio for the inspected wavelength range. In this research a globar opening of 4.0 mm was used, and bolometer openings of 4.0 and 1.2 mm. The largest openings are expected to result in the smearing of the PSF.

Figure 4.7 shows the expected curves for the chosen openings, and figure 4.8 shows the actual measurements. It is immediately clear that the widths are significantly smaller for a smaller opening. A direct comparison between both figures is shown in figure 4.9. The theory and measurements agree very well

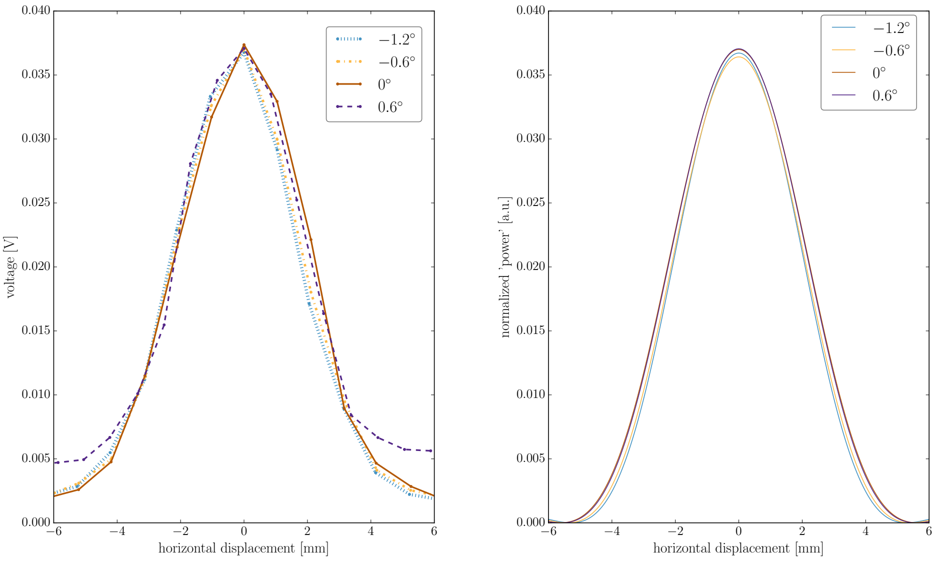

(a) Raw data, collective center. (b) Gaussian fits of each measurement.

Figure 4.5: Comparison of measurements and fitted Gaussians. The fits only take into account the measurement points above 9 mV. The fits do not line up 100%.

above a normalized intensity of 10^{-1}. Below this intensity the influence of the heated diaphragm takes over. The influence of the size of the pinholes is much larger than the polychromaticity of the light, as the modelled curve only takes into account $\lambda = 0.15$ mm.

4.5 Fabry-Pérot Interferometer

A Fabry-Pérot interferometer was used to try to make the broadband light more narrowband. It was placed between the optical system and the detector. Such an interferometer is made of two parallel mirrors, and light that is resonant with this interferometer has a high transmission through it. The other light will not pass through, and therefore the beam is made much more monochromatic.

The transmission of the interferometer used in the measurements is shown in figure 4.10. Resonance measurements of these kinds of interferometers would normally produce a narrower peak, but it is still clear that all frequencies are filtered out, except for around 1.9 THz. This peak corresponds well to the second-highest peak in figure 4.2, and the other peaks have vanished. So

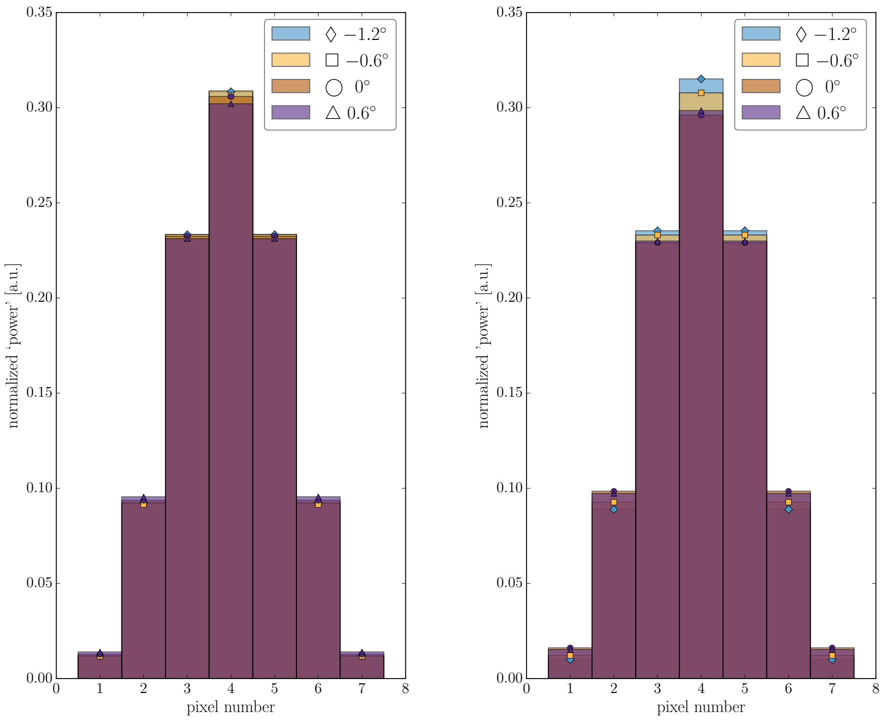

(a) Vertical scan (z-direction). (b) Horizontal scan (x-direction).

Figure 4.6: Nyquist sampled vertical and horizontal scans, with the secondary mirror tilted a certain angle with respect to the zero position. This tilting is only done horizontally, in the x-direction.

indeed a Fabry-Pérot interferometer can be used to make broadband light much more monochromatic.

However, as only a small part of the light is resonant with the interferometer, the total intensity on the detector is much lower than for measurements without the interferometer in the setup. This has a detrimental effect on the signal-to-noise ratio.

Figure 4.11 shows the measurements made with an interferometer in the setup. Because of normalization the measured voltage is not seen in the figure, but it is clear that there is more noise in the 'wings' where an interferomter is present. The maximum measured voltage for the purple curve is 40 mV, whereas the other curves have peaks of only 2–4 mV.

The measurements with the interferometer are a bit narrower, but this positive effect is completely negated by the difficulties in actually getting these measurements. To get an acceptable measurement the amperage of the source

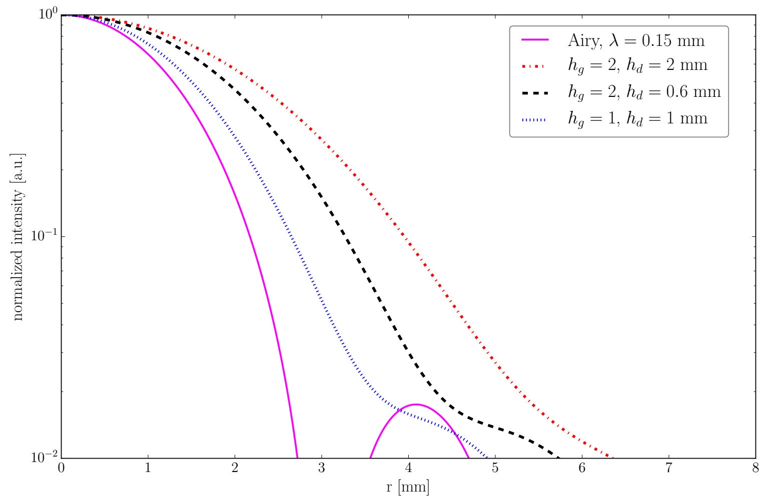

Figure 4.7: Different radii of source and detector openings. The magenta curve is the Airy pattern for $\lambda = 0.15$ mm, the red curve is the expected curve for the measurements ($r = 2$ mm for both globar and detector opening), provided the source is monochromatic with $\lambda = 0.15$ mm. The black curve has $r = 0.6$ mm, which corresponds to a detector opening of 1.2 mm.

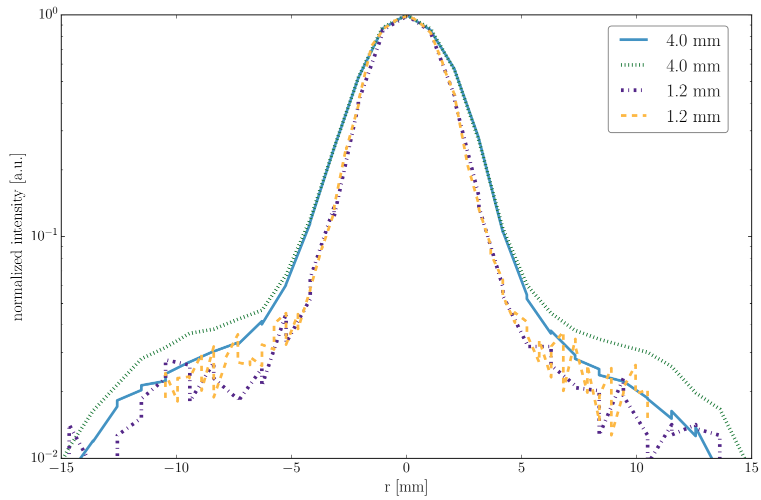

Figure 4.8: Globar opening is 4.0 mm for each measurement, the bolometer has openings (diameter) of 4.0 and 1.2 mm for each two measurements. The size of the opening clearly has a significant effect on the width of the pattern.

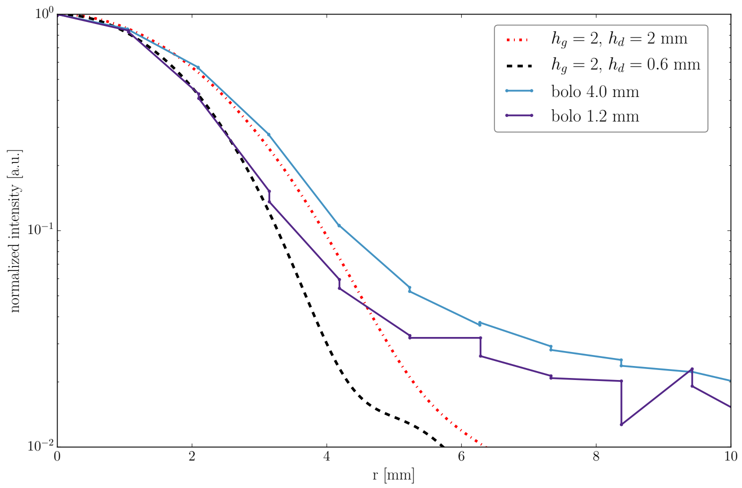

Figure 4.9: Direct comparison of the monochromatic theory in figure 4.7 with the measurements in figure 4.8.

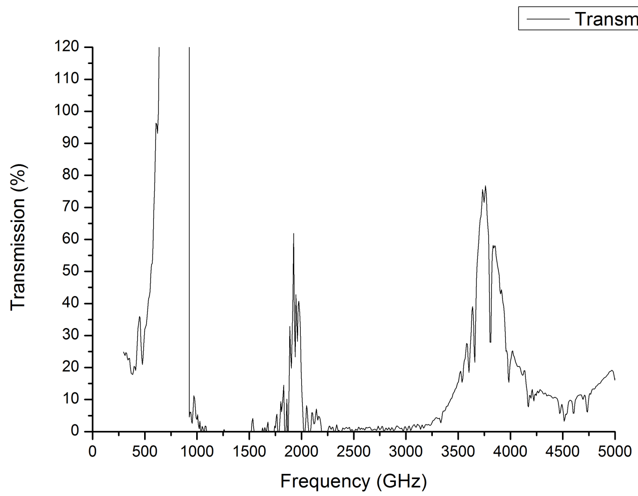

Figure 4.10: The transmission of the Fabry-Pérot interferometer used for the measurements in this section. Frequencies above 3.0 THz can be ignored because the bolometer is not sensitive to those frequencies. The large peak below 1.0 THz is due to division by a signal of almost zero, and can be ignored as well. A large peak at 1.9 THz is left. Figure courtesy of Willem-Jan Vreeling.

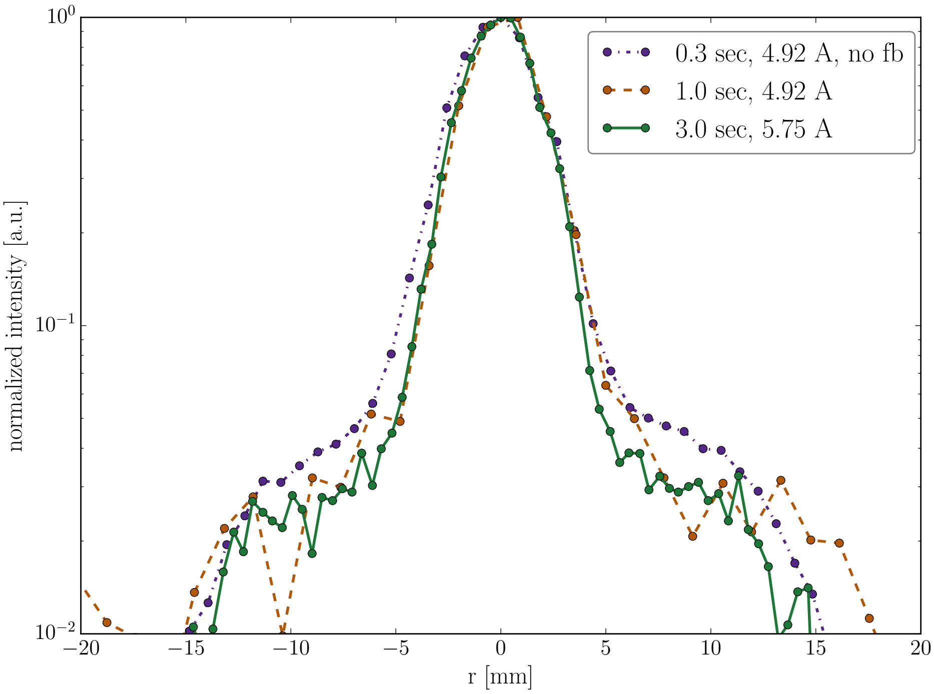

Figure 4.11: The legend shows the settings on the hardware for each measurement. The seconds refer to the settings on the lock-in amplifier, the amperage to the setting on the globar. The purple curve is a measurement without the interferometer, peak at 40 mV. The orange and purple curves are measured with the interferometer. Different settings are on the lock-in amplifier and globar are used, peaks at 2-4 mV. The 'wings' are again because of heating of the diaphragm.

and the settling time on the lock-in amplifier have to be increased significantly. It is not feasible to take all measurements with the globar set on 5.75 A, as that will eventually break the globar. The longer settling time means that a measurement suddenly takes up to 10 times more time, which is unacceptable as the benefits increase is much lower than that.

5. Conclusion

Taking measurements in the far infrared is tough. It is a constant balancing act between source strength, detector sensitivity, and the sizes of the source and detector openings. A globar does not emit as much radiation as a QCL, so the pinhole sizes have to be adjusted accordingly. This means that unfortunately for most experiments it was not possible to measure with very small pinholes, as only the globar was available. However, some very useful results emerged from this.

The atmospheric measurements show that the combined transmission of the atmosphere and the detector result in quite discrete windows. The complete atmospheric spectrum is simplified to three fairly narrow transmission bands centered around 2.0, 2.1, and 2.5 THz.

The experiments with the varying pinhole diameters demonstrate that for large diameters compared to the wavelength, the left-over polychromaticity of the light does not matter anymore. The influence of smearing out of the PSF is much larger. The theory and the measurements agree very well, so the importance of the source and detector window diameters is now much better understood.

Measurements with a Fabry-Pérot interferometer establish once more that these measurements are the result of a trade-off between the many different components discussed above. An increase in monochromaticity can, for the same source, only happen with a decrease in received power.

With the QCL (3.91 THz) the precise alignment of the setup is tested. The fact that a very clear Airy pattern emerges shows that the setup has a (close to) diffraction limited performance at this wavelength, and better performance for the longer wavelengths the other experiments are done with. Any aberrations due to misalignment are magnified for shorter wavelengths, and it shows that this experimental setup has only very slight misalignment.

Finally the most important conclusion is that it is indeed possible to laterally translate a PSF (or indeed any shape) in the focal plane, without changing the PSF itself, over more than 30 mm. It is advisable to redo this set of measurements for the x-direction with a better sampling of the central regions, but the expectation is that this will change the computer's ability to fit a curve to the measurement for the better, and thus make the sampling even more alike.

6. Acknowledgements

This research was done at SRON, a top-class institution in international space research. I was lucky to have found such a cool place to do my master's research, in an inspiring environment with helpful colleagues.

First a big thank you to Gert, who was willing to supervise me even though you knew my struggles with writing and handing in reports on time. Without you I would not have been able to finish this thesis. Your wealth of knowledge ensured that I would not be stuck for too long, and your gentle mentions of the date kept me aware I still had to finish up the writing. :)

Thank you too to Willem-Jan, you were invaluable in setting up the Offner test setup. You taught me how to use different sources, detectors, and even how to use the power supplies. That's hard for someone who had before spent years in an environment where 'applied' means solving a slightly different set of equations, not how to screw teeny-tiny screws into place, level platforms, and mess around with liquid nitrogen. When I would barge in because something stressed me out, you always had time for a chat to calm me down again.

Lastly I want to thank all the people of SRON Groningen who invited me into their midst, helped me with all kinds of smaller and larger problems, and were still interested in my story even after almost two years.

Figure 6.1: We went on SAFARI and found some cool results, but unfortunately no big colorful birds like Kevin. Image from Pixar's UP.

Bibliography

J. Fischer, F. J. Vrba, D. W. Toomey, B. L. Lucke, S.-i. Wang, A. A. Henden, J. L. Robichaud, P. M. Onaka, B. Hicks, F. H. Harris, W. E. Stahlberger, K. E. Kosakowski, C. C. Dudley, and K. J. Johnston. ASTROCAM: An Offner Re-imaging 1024 X 1024 InSb Camera for Near-Infrared Astrometry on the USNO 1.55-m Telescope. In M. Iye and A. F. M. Moorwood, editors, *Instrument Design and Performance for Optical/Infrared Ground-based Telescopes*, volume 4841 of *Society of Photo-Optical Instrumentation Engineers (SPIE) Conference Series*, pages 564–577, March 2003. doi: 10.1117/12.461033.

J. R. Goicoechea and T. Nakagawa. Spica: The next generation infrared space telescope. *EAS Publications Series*, 52:253–258, 1 2011. ISSN 1638-1963. doi: 10.1051/eas/1152041. URL `http://www.eas-journal.org/article_S1633476052000414`.

Eugene Hecht. *Optics*. Addison Wesley, 4th edition, 2002.

V. N. Mahajan. Lecture Notes on Optical Imaging and Aberrations. `http://fp.optics.arizona.edu/opti596C/`, 2011. [Accessed oct 2014].

D. C. Murphy. Two Offner-based IR Camera Optical Designs. *Experimental Astronomy*, 3:141–142, March 1994. doi: 10.1007/BF00430138.

A. Offner. Unit Power Imaging Catoptric Anastigmat. *US Patent 3,748,015*, 1973.

X. Prieto-Blanco, C. Montero-Orille, B. Couce, and R. de La Fuente. Analytical design of an Offner imaging spectrometer. *Optics Express*, 14:9156–9168, October 2006. doi: 10.1364/OE.14.009156.

E. J. J. Schallig. A Step-Integrate Program for the CRIMI, 2013. FIT-stage Master Instrumentation.

B. Swinyard. SPICA, revealing the origins of planets and galaxies. `http://research.uleth.ca/spica/documents/pdf/SPICA_Science_Case_print_version.pdf`, 21 May 2014.

JAXA. SPICA information for researchers. `http://www.ir.isas.jaxa.jp/SPICA/SPICA_HP/research-en.html`, 2014. Accessed february-april 2014.

SAFARI fact sheet. SPICA/SAFARI fact sheet. http://www.ir.isas.jaxa.jp/SPICA/SPICA_HP/fact_sheet/safari-factsheet-v1.pdf, 12 June 2013. Accessed april 2014.

A. Alignment

The theodolite works by sending out an image of green crosshairs. It is oriented perpendicularly to a plane mirror when the crosshairs are reflected to the center of the theodolite. This is not possible with curved mirrors, therefore aligning this setup involves some work-around. The theodolite is assumed to be able to be aligned in the xy-plane with its bull's eye level, in which case $\theta = 90°$. See figure A.1 for the coordinate system used.

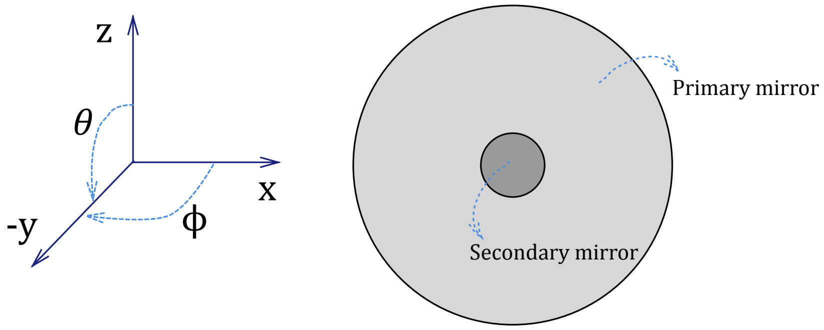

Figure A.1: Coordinate system with the mirror orientations as reference, where the small mirror is seen from the back. z is upwards, x to the right and y towards the mirrors. θ is the angle in the yz-plane, ϕ is the angle in the xy-plane. This is the same figure as figure 3.3.

Below the complete recipe for alignment of the primary and the big secondary is given. Figure A.2 is the same process in pictures.

1. The primary mirror is secured to the optical table, aligned as much as possible to the grid of holes in the table.
2. The plane mirror is pressed to the back of the primary mirror; with the theodolite at t_1 the crosshairs (the beam represented by l_1) are found. This is to find the horizontal orientation of the primary mirror. The vertical orientation of the mirror can be adjusted until the theodolite reads horizontal ($\theta = 90°$).
3. Keeping the theodolite on the same spot at t_1, rotate it a certain angle (e.g. 90°) and align another plane mirror. With this the orientation of the primary mirror is kept when moving the theodolite.

4. Now move the theodolite over to roughly the center of the primary mirror, at t_2, on an xz-stage, find the crosshairs again (l_2) and rotate 90° back to look at the mirror.

5. Align precisely by looking at the edges of the mirror through the theodolite and noting the angles. When those angles α are the same left-right and up-down, the theodolite points exactly at the center of the mirror. DO NOT move the theodolite itself, use the xz-stage. Routinely check with the plane mirror that the angle is still 90°.

6. The theodolite is now positioned along the principal axis; do not move the theodolite anymore. Send out a collimated beam from the theodolite. Find the focal point (the circle of least confusion) with e.g. a beam splitter and touch it with the pointing mechanism. This should be 500 mm from the mirror.

7. Position the secondary mirror on a xyz-stage such that its center is (almost) touching the pointer.

8. Press a small plane mirror to the flat back of the secondary. Give the secondary the same orientation as the primary by rotating it until the crosshairs are again in the center of the theodolite.

9. Lastly check the edges of the secondary mirror and move the mirror until the angles left-right and up-down are again equal.

For the second secondary mirror the alignment was based on the position of the first secondary. As it was a few months later, the referencing equipment had already been stored away.

(a) The orientation of the primary mirror is again found and transferred to a reference plane mirror, as described in steps 2 and 3.

(b) Place the pointer such that it (almost) touches the center of the secondary mirror. Switch out the mirrors, move the xyz-stage until the center of the new mirror corresponds to the pointer.

(c) Place the theodolite just slightly off-center (e.g. to the left) from the primary mirror, parallel to the principal axis. Remove the secondary mirror from the attocube system and stick a small plane mirror on it such that it is visible to the theodolite around the suspension.

(d) Again give the secondary mirror the same orientation as the primary by rotating it until the crosshairs are reflected back to the center of the theodolite.

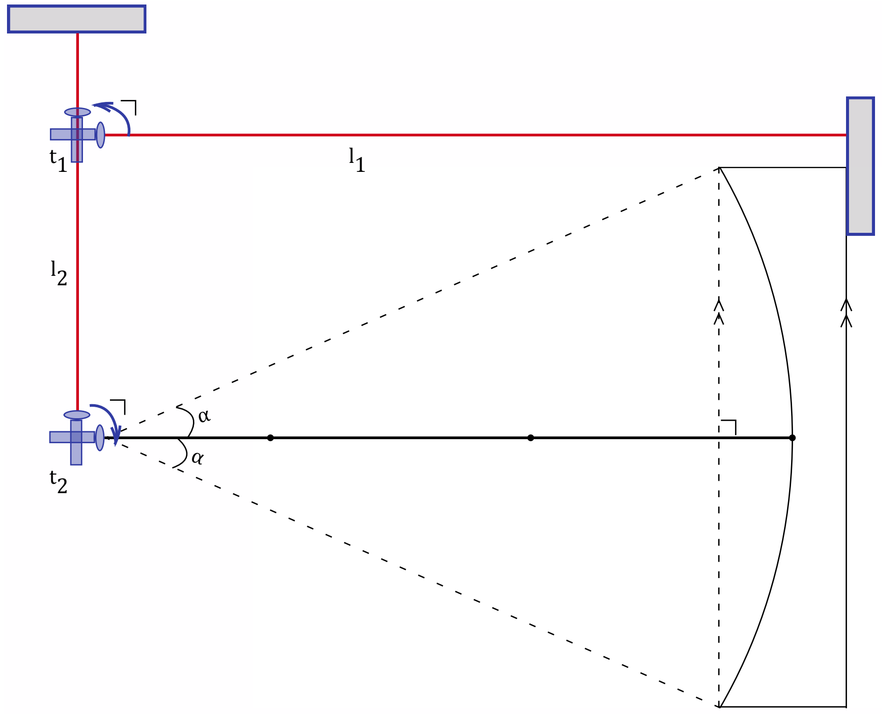

(a) Step 1 through 5.

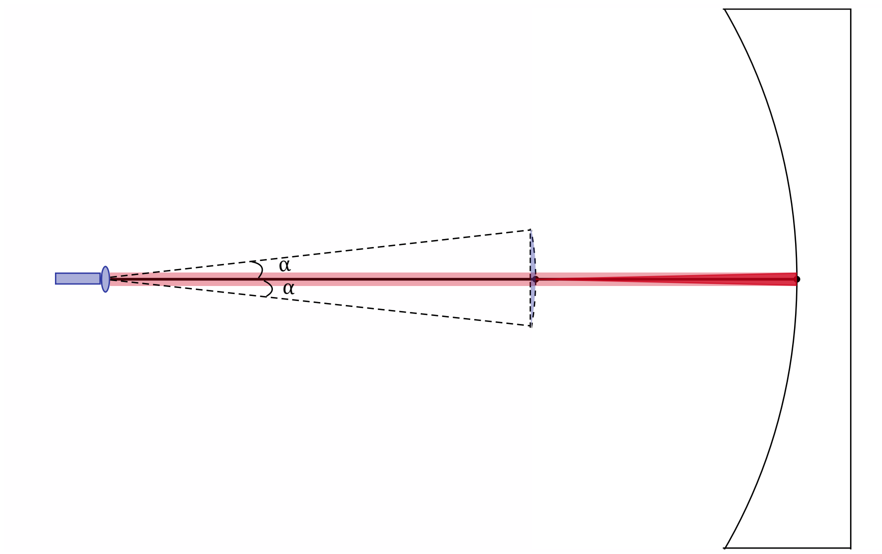

(b) Step 6 through 9.

Figure A.2: Alignment with theodolite. Top-down view.

(e) Write down the attocube system's positions for both axes for future reference, as this is the zero position. Put back the convex mirror.

The pointer gives the xyz-position and with the theodolite the right orientation is found. This can be tested with a light beam a distance d from the principal axis, at the same distance from the mirror as point C (see figure A.3). If the light converges at a distance d on the other side of point C, the correct orientation has been found.

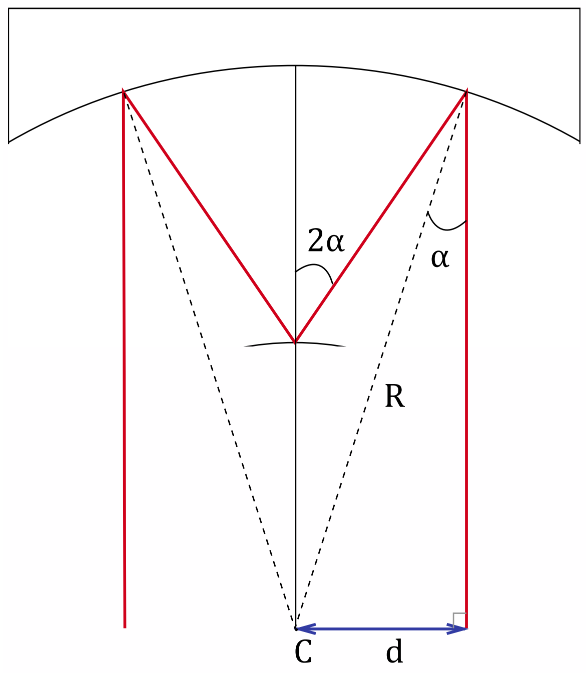

Figure A.3: Method for testing the extent of success in aligning the setup. If light from a point source at a distance d from C converges on the other side with the same distance d from point C, the alignment is correct. This is the same figure as figure 3.5 (a).